


Asymmetric hierarchical acoustic absorber at exceptional point: A loss-induced eigenvalues degeneracy system

Zichao Guo, Zhendong Li, Kexin Zeng, Xinying Lu, Jie Ye, and Zhonggang Wang ^{*}

School of Traffic & Transportation Engineering, Central South University, Changsha, Hunan 410075, China;

Key Laboratory of Traffic Safety on Track, Ministry of Education, Changsha, Hunan 410075, China;

and National & Local Joint Engineering Research Center of Safety Technology for Rail Vehicle, Changsha, Hunan 410075, China



(Received 30 October 2023; revised 27 February 2024; accepted 29 February 2024; published 19 March 2024)

In the realm of non-Hermitian physics and noise-control engineering, exceptional points (EPs), where two or more discrete eigenvalues and the corresponding eigenvectors coalesce, have garnered significant attention. Here, we present an integrated approach that fuses intrinsic loss through loss-factor modulation with extra airflow loss via the rainbow-trapping effect to reach the EP in a loss-only system. Moreover, by introducing the hierarchical concept with graded dimension and scaling effect, the asymmetric hierarchical acoustic metamaterials achieve efficient broadband sound absorption with absorption coefficients exceeding 0.7 over 400 Hz at low frequencies within the deep-subwavelength scale. This is evidenced through both numerical simulations and experimental results, showcasing near-total reflection from one side and high absorption from the other. This study presents a loss-induced hierarchical design approach for manipulating acoustic waves, offering insights for advancements in acoustic metamaterials and noise-control applications.

DOI: [10.1103/PhysRevB.109.104113](https://doi.org/10.1103/PhysRevB.109.104113)

I. INTRODUCTION

Notions drawn from unidirectional zero-reflection propagation where incident waves are reflectionless in only one direction have attracted considerable attention [1–5]. One paradigmatic and extensive application of unidirectional response is noise-control engineering [6–17]. In recent years, the emergence of acoustic metamaterials endows a more efficient capability for acoustic wave manipulation [18–22]: for example, harnessing nonlinearities, moving media, spatiotemporal modulation, and nonlinear bianisotropy to realize nonreciprocal wave propagation [23–26]. Breaking the time-reversal symmetry to create acoustic nonreciprocity remains a formidable challenge. Herein, a physical concept that achieves asymmetric wave propagation in non-Hermitian systems, also known as parity-time (PT) symmetric systems, is termed the exceptional point (EP). This occurs when two or more discrete eigenvalues and their corresponding eigenvectors coalesce [27–38].

The acoustic system offers a feasible and versatile platform for the EP, allowing for the control of non-Hermitian parameters in various forms [27]. To date, physical realizations of EP for unique wave manipulation generally originate from two categories. One approach is to utilize PT-symmetric synthetic media, which precisely tames the balance of loss and gain media [34–36]. To achieve effective acoustic-gain media, experimental approaches with active elements are employed, such as energy conversion of thermoacoustics [27] or electroacoustics [36]. Yet, the shortage of natural acoustic-gain materials exists and uneasily controlled gain media poses

a significant challenge. This challenge can greatly amplify the complexities and instabilities of the systems. An alternative method for achieving the EP involves controlling the unbalanced loss factors of passive non-Hermitian systems. At the EP, intriguing properties such as unidirectional zero reflection can also be observed [39–42]. In these passive systems, the EP can be synthesized by tuning the structural parameters of different sections or adding the proper loss media. However, the asymmetric responses for EP solely by modulating structural parameters are limited due to precise modulation and fewer available parameters. Incorporating additional lossy media into the system is a viable approach, but it may lead to a relatively sophisticated design of the system [27,31].

One observes that acoustic systems are typically nonconservative, where losses are ubiquitous. In such a case, we consider the rainbow-trapping effect, which has the potential to enhance dissipation losses by confining the acoustic field to a single resonator at resonance frequency [43–45]: hence, a paradigm for realizing unidirectional reflectionless propagation for sound, which combines intrinsic loss through loss-factor modulation with additional airflow loss via the rainbow-trapping effect to achieve the EP in a loss-only system. Consequently, the parameter space utilized for synthesizing EP is expanded without additional loss materials. Furthermore, the concept of hierarchy with graded dimension and scaling effect is introduced [46–48], and we observe its signature, trapping positions exhibit extensible frequency-cascade behavior. Meanwhile, the development of additive manufacturing (AM) technology provides a straightforward method for effectively fabricating acoustic metamaterial systems with non-Hermitian modulation, even in more complex and fine geometries [49,50].

^{*}wangzg@csu.edu.cn

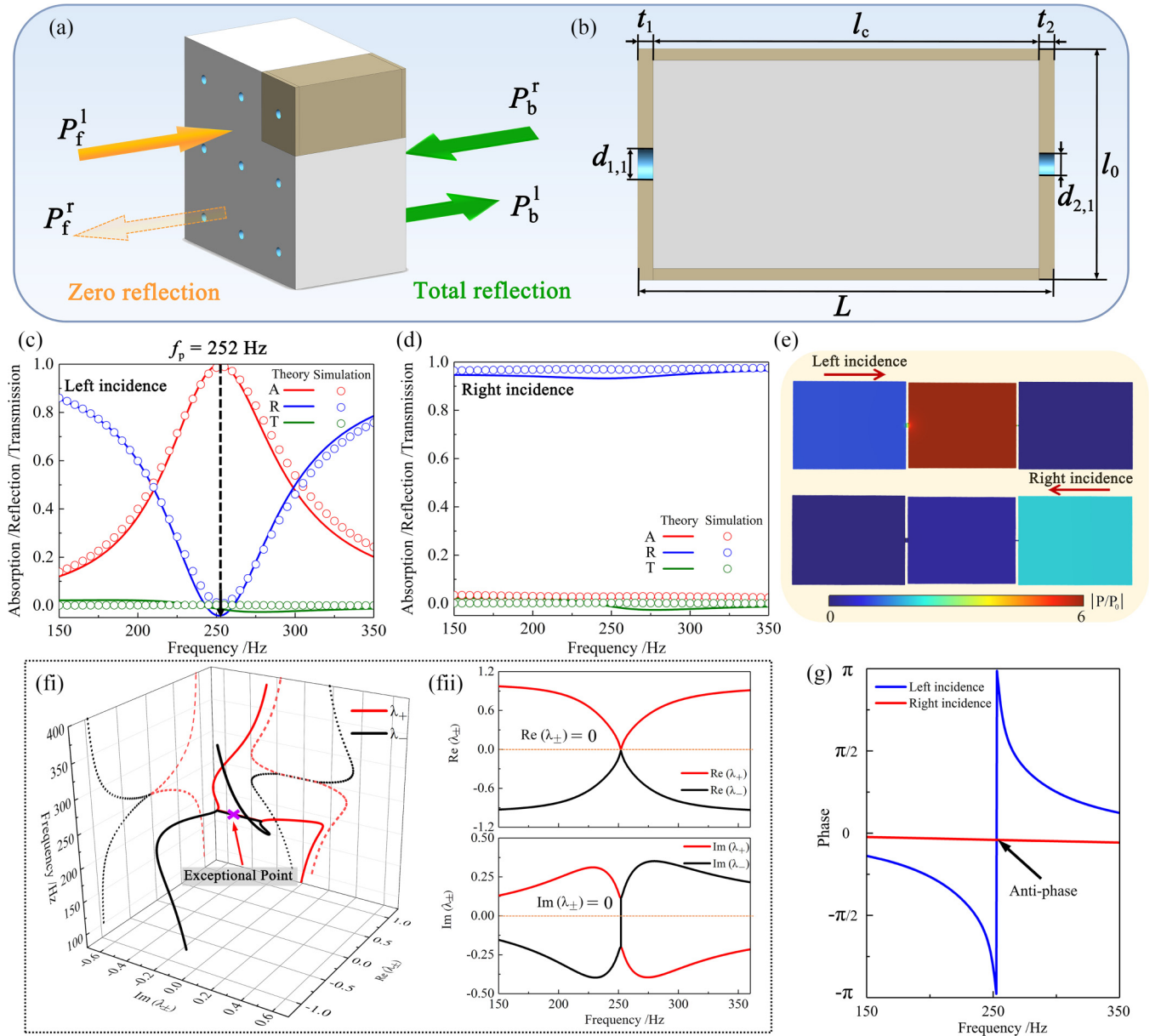


FIG. 1. Asymmetric absorption via exploiting the concept of exceptional point. (a) Schematic view of the compact prototypical absorber. (b) A cross-sectional view of the periodic unit. (c), (d) Absorption, reflection, and transmission coefficients of asymmetric absorbers when the sound waves radiate from the left and right sides, respectively. (e) Distribution of sound pressure at 252 Hz from the left and right sides. (f) Trajectories (i) of eigenvalues (λ_{\pm}), and (ii) corresponding real and imaginary parts under the operating frequency range. (g) Theoretically calculated reflection phases from the left and right sides, respectively.

In this study, we introduce an approach that EP can be synthesized by asymmetric hierarchical acoustic metamaterials (AHAM) with integrating rainbow trapping and intrinsic loss. Specifically, the experimental demonstrations and numerical calculations verified the asymmetric performance, achieving an absorption band exceeding 400 Hz within a minimum coefficient of 0.7 and near-total reflection from the opposite incidence at low frequency in the deep-subwavelength scale. The proposed metamaterials have asymmetric absorption characteristics, which have potential applications in various scenarios, such as acoustic indoor walls, functional furniture, etc. [51–53]. Overall, the hierarchical design presents a compact asymmetric absorber for the functionality

of asymmetry feature, deep-subwavelength scale, and broadband absorption spectrum. This design provides a promising approach for acoustic metamaterial research and noise-control engineering.

II. ASYMMETRIC SOUND-ABSORBING MECHANISM

A. Theoretical analysis

A conceptual schematic representation of a prototype structure characterized by asymmetry is depicted in Fig. 1(a). This compact configuration comprises two microperforated plates (MPPs) with high dissipation-loss properties, connected to a square cavity. When acoustic waves impinge from

the left to right direction, they are nearly or totally absorbed, realizing the quasiperfect or perfect absorption. Conversely, when the waves approach from the opposite direction, total reflection occurs with no absorption, exhibiting asymmetric absorption. An asymmetric sound absorber is sketched in Fig. 1(b). The geometrical parameters l_0 and L represent the length and total thickness of the asymmetric unit cell, respectively. $d_{1,1}$ and $d_{2,1}$ refer to the diameters of microperforations related to the left and right MPPs; t_1 and t_2 refer to the thickness of corresponding MPPs. l_c denotes the distance of the cavity.

To illustrate the acoustical performance of this dual-port asymmetric system in Fig. 1(a), we employ the parallel transfer-matrix method (TMM) to express the acoustic response of asymmetric absorbers [54], calculated as

$$M_{\text{total}} = \begin{bmatrix} A & B \\ C & D \end{bmatrix} = \frac{-1}{\sum r_x Y_{21}^x} \times \begin{pmatrix} \sum r_x Y_{21}^x & -1 \\ \sum r_x Y_{22}^x \sum r_x Y_{11}^x - \sum r_x Y_{12}^x \sum r_x Y_{21}^x - \sum r_x Y_{11}^x & \end{pmatrix}, \quad (1)$$

where Y^x and r_x refer to the admittance matrix and area ratio of each asymmetric unit with the parallel absorbers, respectively. The transfer matrix of a single asymmetric unit for the sound wave radiating from the left port is expressed as

$$M = M_{\text{MPP1}} M_{\text{cavity}} M_{\text{MPP2}}, \quad (2)$$

where M_{MPP1} and M_{MPP2} describe the matrices of the plates, respectively; M_{cavity} represents the matrix of the cavity, calculated as

$$M_{\text{MPP}} = \begin{bmatrix} 1 & Z_{\text{MPP}} \\ 0 & 1 \end{bmatrix} \quad (3)$$

$$M_{\text{cavity}} = \begin{bmatrix} \cos(kl_c) & jZ_0 \sin(kl_c) \\ jZ_0 \sin(kl_c)/Z_0 & \cos(kl_c) \end{bmatrix}, \quad (4)$$

where $Z_0 = \rho_0 c_0$ is the characteristic impedance of the air medium, where ρ_0 and c_0 are, respectively, the density and velocity of sound in air. $k = \omega/c_0$ represents the wave number and ω denotes the angular frequency of the incident sound wave. Z_{MPP} denotes the impedance of MPP and is expressed as [55]

$$Z_{\text{MPP}} = \frac{j\omega\rho_0 t_1}{\sigma_{1,x}} \left[1 - \frac{2B_1(\eta\sqrt{-j})}{(\eta\sqrt{-j})B_0(\eta\sqrt{-j})} \right]^{-1} + \frac{\sqrt{2}\mu\eta}{\sigma_{1,x}d_{1,x}} + \frac{0.85j\omega\rho_0 d_{1,x}}{\sigma_{1,x}}, \quad (5)$$

where $\eta = d_{1,x}\sqrt{\omega\rho_0/4\mu}$ represents the ratio of the diameter of the perforation to the thickness of the viscous boundary layer. B_0 and B_1 are the zeroth- and first-order Bessel functions, respectively; $\mu(1.8 \times 10^{-5} \text{ Pa} \cdot \text{s})$ is the dynamic viscosity. The porosity $\sigma_{1,x}$ is calculated as the ratio of the area of the perforation to that of the corresponding plate. Hence, the corresponding scattering coefficients of the asymmetric

TABLE I. Geometric parameters of prototypical structure (unit: mm).

	$d_{1,1}$	t_1	$d_{2,1}$	t_2	l_c	l_0
Asymmetric prototype	1.5	1	0.35	1	38	30

absorber can be given as [31]

$$T = \frac{2e^{jkL}}{A + B/Z_0 + CZ_0 + D}, \quad (6)$$

$$R_l = \frac{A + B/Z_0 - CZ_0 - D}{A + B/Z_0 + CZ_0 + D}, \quad (7)$$

$$R_r = \frac{-A + B/Z_0 - CZ_0 + D}{A + B/Z_0 + CZ_0 + D}, \quad (8)$$

where T is the transmission coefficient; R_l and R_r denote the reflection coefficients for sound radiated from the left and right sides, respectively. The asymmetric absorption performance from different ports can be derived as

$$A_l = 1 - |R_l|^2 - |T|^2, \quad (9)$$

$$A_r = 1 - |R_r|^2 - |T|^2 \quad (10)$$

Furthermore, the scattering characteristic of this asymmetric two-port system is described by its scattering matrix. The forward (left) and backward (right) ingoing acoustic waves are denoted by P_f^l and P_b^r , while the outgoing sound waves are expressed as P_f^r and P_b^l , respectively. The relation is expressed by

$$\begin{bmatrix} P_f^r \\ P_b^l \end{bmatrix} = \begin{bmatrix} T & R_l \\ R_r & T \end{bmatrix} \begin{bmatrix} P_b^r \\ P_f^l \end{bmatrix}. \quad (11)$$

The eigenvalues of the scattering characteristic can be described as a 2×2 matrix, given by

$$\lambda_{\pm} = T \pm \sqrt{R_l R_r}. \quad (12)$$

Moreover, the finite-element method (FEM) is conducted in COMSOL MULTIPHYSICS, and the pressure-acoustic module and the thermoviscous-acoustic module are employed to simulate the proposed dual-port acoustic system. Detailed procedures for the simulation are shown in Appendix A. This proposed dual-port acoustic system reveals advanced wave manipulation within compact thickness and stabilized geometrical configuration.

B. Extreme absorption asymmetry at the exceptional point

As a proof of concept, this compact sound absorber exhibits extreme asymmetric absorption characteristics from different directions of incident waves, as shown in Figs. 1(c) and 1(d). The red, blue, and green lines (scatters) represent absorptance, reflectance, and transmittance, respectively. The geometrical parameters are listed in Table I. The theoretical calculations and numerical simulations are in good agreement. Quasiperfect sound absorption (99.7%) occurred at 252 Hz in the left incidence, while the sound waves are nearly total reflection (98.7%) from the right side. This absorber with a

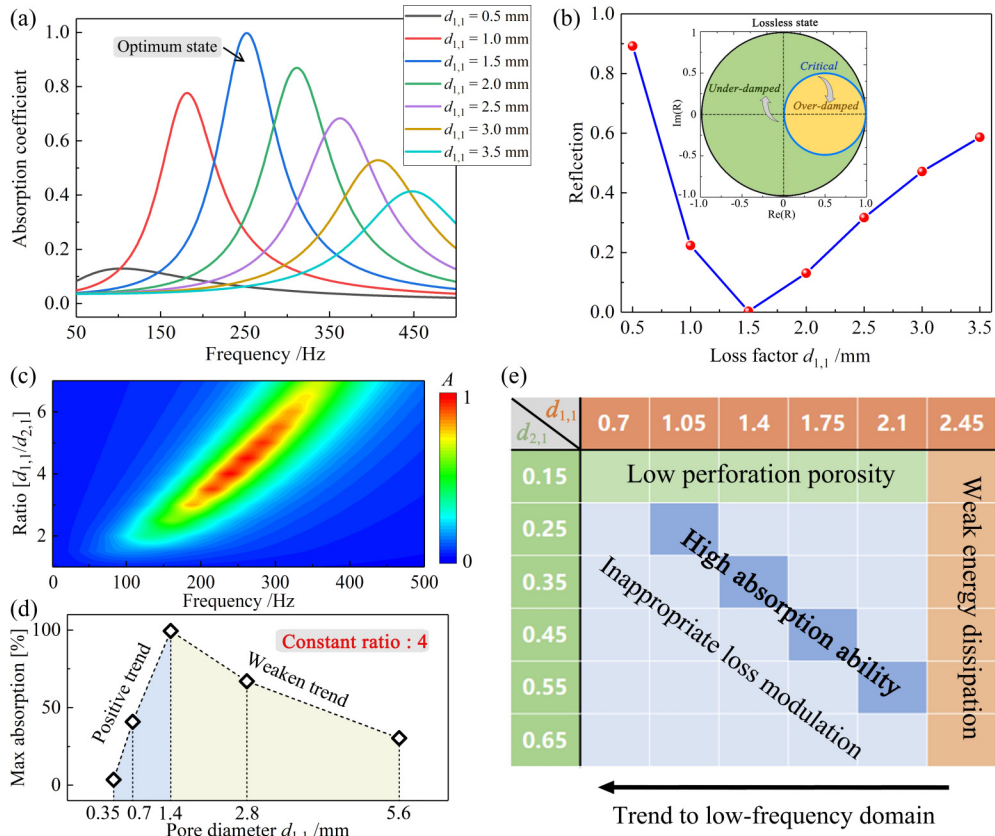


FIG. 2. Loss-factor modulation of the asymmetric sound absorber. (a) Sound-absorption performance of different loss factors $d_{1,1}$, represented by the colored lines. (b) Reflection coefficient observation of absorbers' peak values. The Argand diagram of the complex reflection coefficient. The reflection attains a minimum value of 1.5 mm. (c) Absorption spectrum with different ratios of $d_{1,1}/d_{2,1}$. (d) The plot of percentage increase in the maximum absorption for constant ratio with different perforation sizes. (e) An overall summary of the absorption of different perforation pores.

thickness of 40 mm exhibits excellent low-frequency sound-absorption performance in deep-subwavelength scale (nearly $1/34$) of the operating wavelength at 1.35 m. To elucidate the absorbing mechanisms of the dual-port acoustic system, the sound-pressure field distributions $|P/P_0|$ are displayed by finite-element (FE) simulations in Fig. 1(e). The P and P_0 represent scattered acoustic pressure and incident acoustic pressure, respectively. In this scenario, significant energy dissipation occurs at 252 Hz when sound waves radiate from the left side, resulting in a notable difference in acoustic-pressure amplitude. Conversely, in the opposite direction, the sound waves experience nearly total reflection, signifying minimal energy dissipation.

This two-port acoustic absorber exhibits extreme asymmetric performance in general non-Hermitian systems, which is realized under the combined action of loss factors. By leveraging the interplay of loss factors among the different MPPs and the distance of the cavity, we can attain the exotic property of unidirectional zero reflection. To further understand the physics, we investigate the eigenvalues of the scattering matrix. The eigenvalues λ_{\pm} of Eq. (12) coalesce (252 Hz) under a system parameter variation, exhibiting a certain point called EP, as shown in Fig. 1(f). There is only one point in this plot where both the real parts are the same and the imaginary parts coincide [56–59]. Specifically, EP is accessed when the

real parts $\text{Re}(\lambda_{\pm})$ and corresponding imaginary parts $\text{Im}(\lambda_{\pm})$ of eigenvalues are equal to zero simultaneously [Fig. 1(f)]. Meanwhile, the phases of the reflection for the left and right incidence are shown in Fig. 1(g). The asymmetric system undergoes the phase transition from the left side, and the corresponding reflection vanishes due to the existence of EP, contributing to realizing unidirectional reflection. It should be emphasized that the complex eigenvalues λ_{\pm} of this two-port acoustic system are only hinged on the loss factors instead of modulating the balance of loss and gain, which is different from the PT-symmetric system where system Hamiltonian switches abruptly from real to complex spectrum [30,35,36]. Hence, by leveraging the concept of EP in wave manipulation for the proposed design, the extreme asymmetric absorption is realized.

C. Loss-factor modulation

The zero reflection and perfect absorption can be realized by tailoring the EP of the asymmetric absorber. The geometrical asymmetric and unbalanced loss factors are crucial for the sufficient synthesis of EP. Tuning the intrinsic loss of the systems is an effective approach for achieving EPs, which has been employed in previous studies [31,60,61]. Our structure offers a simpler alternative by modulating the loss

factors through the plate parameters, eliminating the relatively sophisticated geometrical configuration. Here, we first analyze the diameter $d_{1,1}$ of the left MPP as an example to approach the EP. Note that other loss factors are described in Appendix B. The effect of this geometric factor is explored to further realize the absorption properties based on the condition of keeping other geometric parameters unchanged.

Figure 2(a) illustrates the absorption spectrum from the left port with different $d_{1,1}$ of the left MPP. The colored lines exhibit the absorption characteristics of enhancement and subsequent attenuation, while the diameter of the loss factor maintains a steadily increasing trend. The absorption performance is represented by the blue lines attached to the optimum state. The reflection coefficient observation of absorption peak values is presented in Fig. 2(b), indicating a loss-induced coupling behavior. Note that the minimum value of reflection is observed at $d_{1,1} = 1.5$ mm. The difference trend is attributed to the switching of the damping state, shown in the Argand diagram of the complex reflection coefficient of Fig. 2(b) [7]. When the diameter of $d_{1,1}$ exceeds 1.5 mm, the acoustic system exhibits an underdamped state, which illustrates insufficient energy loss. On the opposite, the overdamped state exhibits excess loss energy when the $d_{1,1}$ less than 1.5 mm. Hence, the EP occurs exactly at the transition (critical state) between the under- and overdamped coupling state [14–16,62]. So, we can get the perfect absorption (PA) originating from the EP via elaborately decorating the loss factor.

We further analyze the ratio of the asymmetric size of the perforation. Figure 2(c) shows the absorption spectrum via tuning the diameter $d_{1,1}$ while maintaining a constant diameter $d_{2,1}$. In line with the principles of Helmholtz resonance, larger pore size enables increased airflow, reducing the effective

mass and stiffness of the vibrating air. This, in turn, leads to a decrease in absorption intensity. Further, Fig. 2(d) illustrates the percentage increase in the maximum absorption to different perforation diameters with constant perforation ratios. In the studied cases, absorption increases until reaching its maximum at a 1.4-mm cutoff diameter, then weakens. The variation in absorption intensity with a constant perforation ratio is mainly due to inappropriate acoustic parameter selection, resulting in low porosity and weak energy dissipation. Figure 2(e) presents a chart that illustrates the various geometries and studies conducted for the proposed absorbers. This mechanism also serves as a valuable design guideline for other homogeneous structures. Therefore, this construction, simple yet performance effective, provides highly efficient sound-absorption capabilities while occupying a more compact footprint for asymmetric performance.

III. ASYMMETRIC PROPERTY OF HIERARCHICAL CONFIGURATION

A. Broadband sound absorption

The proposed design guideline and physical mechanism based on loss-induced effects can achieve perfect low-frequency sound-absorption characteristics. However, the asymmetric responses solely by carefully modulating structural parameters are limited [the appropriate loss occupies a small proportion in the tunable parameter spectrum shown in Fig. 2(e)], and incorporating lossy media into the system may lead to a relatively complex design of the system. Therefore, we propose an asymmetric wideband sound-absorption design that incorporates a hierarchical concept with infinite evolution and self-similar characteristics. This structural design offers

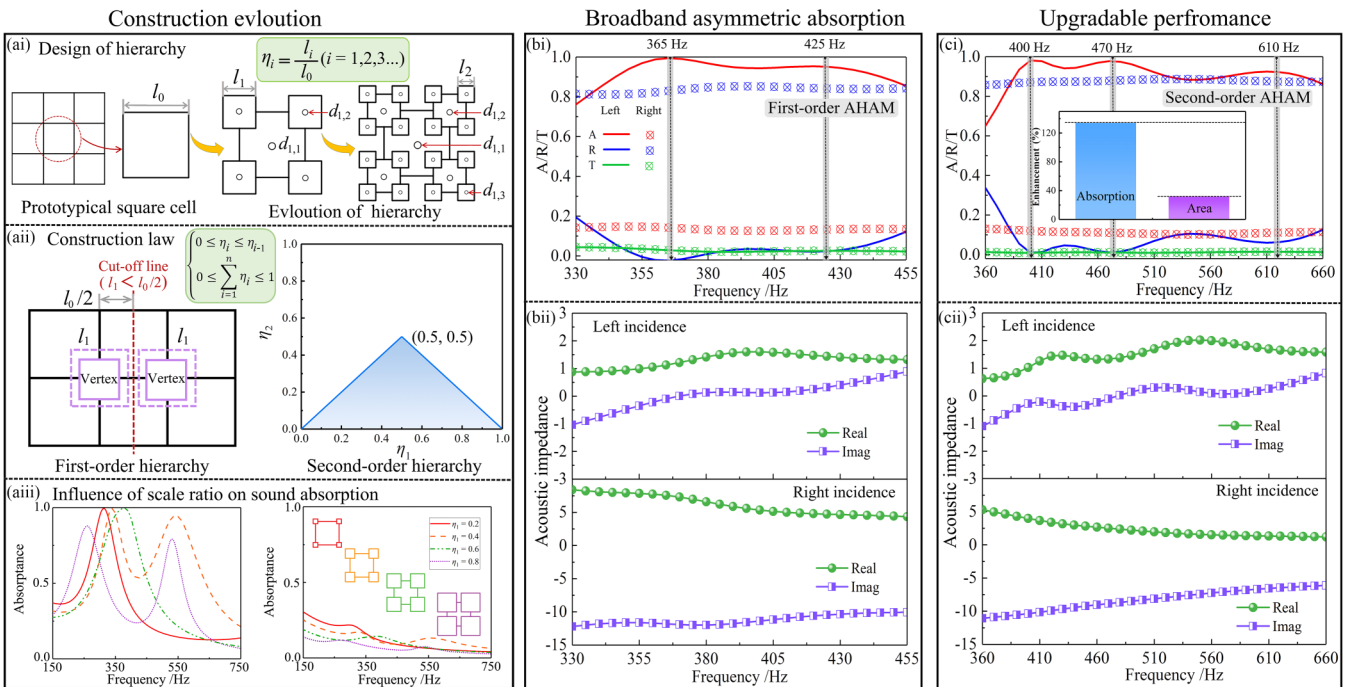


FIG. 3. Design and sound-absorption properties of AHAM. (a) Evolution of the construction of (i) hierarchy design, (ii) construction law, and (iii) the influence of scaling ratio on sound absorption. (b) Broadband asymmetric absorption of (i) first-order AHAM, and (ii) its corresponding acoustic impedance. (c) Upgradable absorption performance of (i) second-order AHAM, and (ii) its acoustic impedance.

TABLE II. Geometric parameters of first- and second-order AHAMs (unit: mm).

	$d_{1,1}$	$d_{1,2}$	$d_{1,3}$	t_1	$d_{2,1}$	$d_{2,2}$	$d_{2,3}$	t_2	l_c	l_0	η_1	η_2
First order	1.6	1.0		1	0.6	0.45		1	48	25	0.5	
Second order	1.6	1.0	0.7	1	0.3	0.3	0.3	1	48	25	0.5	0.25

an integrated approach to introduce additional airflow loss via the rainbow-trapping effect, facilitating the synthesis of the EP.

The vertex-based hierarchy (VH) comprises a traditional multicellular square tube and vertex units, which are periodically arranged with customized patterns, as shown in Fig. 3(ai). Note that the square structure depicted in Fig. 1 is the original cell. Higher-order VH is created by replacing the vertices of the previous order with smaller square cells and continuously evolving to generate an i th-order VH. In this paper, we define this proportional relationship as scaling ratios

$$\eta_i = \frac{l_i}{l_0} (i \in N^*), \quad (13)$$

where l_i refers to the smallest length of i th-order VH. The schematic view of geometric parameters of microperforations from one side ($d_{1,1}$, $d_{1,2}$, and $d_{1,3}$) is also plotted in the corresponding hierarchical configuration. And, the other side is expressed as $d_{2,1}$, $d_{2,2}$, and $d_{3,3}$. Meanwhile, the hierarchical evolution process is shown in Fig. 3(aii), from which the geometric compatibility conditions required for VH evolution can be obtained. The two cells formed at adjacent vertices (purple solid and dotted lines) will expand to the red dashed line if the geometric constraints are not restricted, which will result in edge overlap between vertex cells. Hence, for the i th hierarchical order,

$$\begin{aligned} 0 &\leq l_i \leq l_{i-1} \\ 0 &\leq \eta_i \leq \eta_{i-1}. \end{aligned} \quad (14)$$

When this equation is extended to the entire VH, we can obtain

$$0 \leq \sum_{i=1}^n \eta_i \leq \eta_{i-1}. \quad (15)$$

And eventually, the construction law of first- and even high-order VH is provided by substituting Eq. (13) to Eq. (15):

$$\begin{aligned} 0 &\leq \eta_i \leq \eta_{i-1} \\ 0 &\leq \sum_{i=1}^n \eta_i \leq 1. \end{aligned} \quad (16)$$

Based on this, the two-dimensional range of values for the scaling ratio of second-order VH are obtained and are given in Fig. 3(aiii). Except for the design principle of hierarchy, the scaling ratio also generates a significant influence on sound absorption. The numerically calculated results with typical scale ratios of first-order asymmetric hierarchical acoustic metamaterial are exhibited in Fig. 3(aiv). Inappropriate hierarchical scaling ratios are manifested as a weak coupling effect and poor absorption property. The first-order AHAM obtains two coupled peaks and exhibits increasing coupling strength when the value of scaling ratio η_1 nears 0.5. In

our scheme, the high-efficiency and broadband absorption of AHAM is enabled by cooperation in two dimensions: loss-induced extremely asymmetric absorption in the wave propagation direction; coherent coupling for the broadband absorption between asymmetric resonators is realized in the vertical direction of the incidence sound wave.

After considering the process of hierarchical evolution, we investigate the asymmetric absorption of first-order AHAM with $\eta_1 = 0.5$ in Fig. 3(bi). The solid lines and scatters represent the coefficients of absorption, reflection, and transmission when the sound waves radiate from the left and right sides, respectively. The high-efficiency broadband sound absorption ($A \geq 0.8$) is obtained from 335 to 465 Hz, and exhibits deep-subwavelength ($1/20$) property of the operating wavelength at 1.024 m. Two strongly coupled absorption peaks appear at 365 and 425 Hz, indicating less fluctuation of acoustic impedance and smooth impedance-matching behavior from the left side [shown in Fig. 3(bii)]. On the contrary, when the sound waves propagate from the right side, the real and imaginary parts of acoustic impedance exhibit large intervals compared to the impedance-matching condition (structural impedance is well matched with air medium), resulting in weak absorption characteristics. Further, an upgradable performance is achieved in Fig. 3(c) via utilizing second-order AHAM. The bandwidth is increased to 305 Hz, and three absorption peaks are generated due to the coherent coupling effect. It should be noted that the absorption performance is enhanced by 134.6% compared to first-order AHAM, while the size of second-order AHAM is increased by 32.1%. The enhancement mechanism stems from the scaling effect [46,47]. As the hierarchy evolves, the vertex units acquire a smaller area, resulting in a wider absorption band in the higher-frequency range. As a result, this upgradable design achieves a harmonious balance between compactness for lightweight equipment and broadband-absorbing performance. It is crucial to note that the broadband performance is greatly affected by the coupling strength linked to the first resonance frequency of each unit, as outlined in Appendix C. The corresponding acoustic impedance of second-order AHAM is displayed in Fig. 3(cii). The impedance matching is expanded to a wider frequency range from the left side, whereas the acoustic impedance remains distant from the matching condition on the opposite side. Hence, the AHAM exhibits continuously expanding frequency-cascade behavior due to the existence of scaling ratio and self-similar configuration of graded dimensions. The geometric parameters are listed in Table II.

B. Physical mechanism

To characterize the broadband sound-absorbing properties and the underlying mechanisms of AHAM, we investigated the sound pressure, acoustic particle velocity distributions,

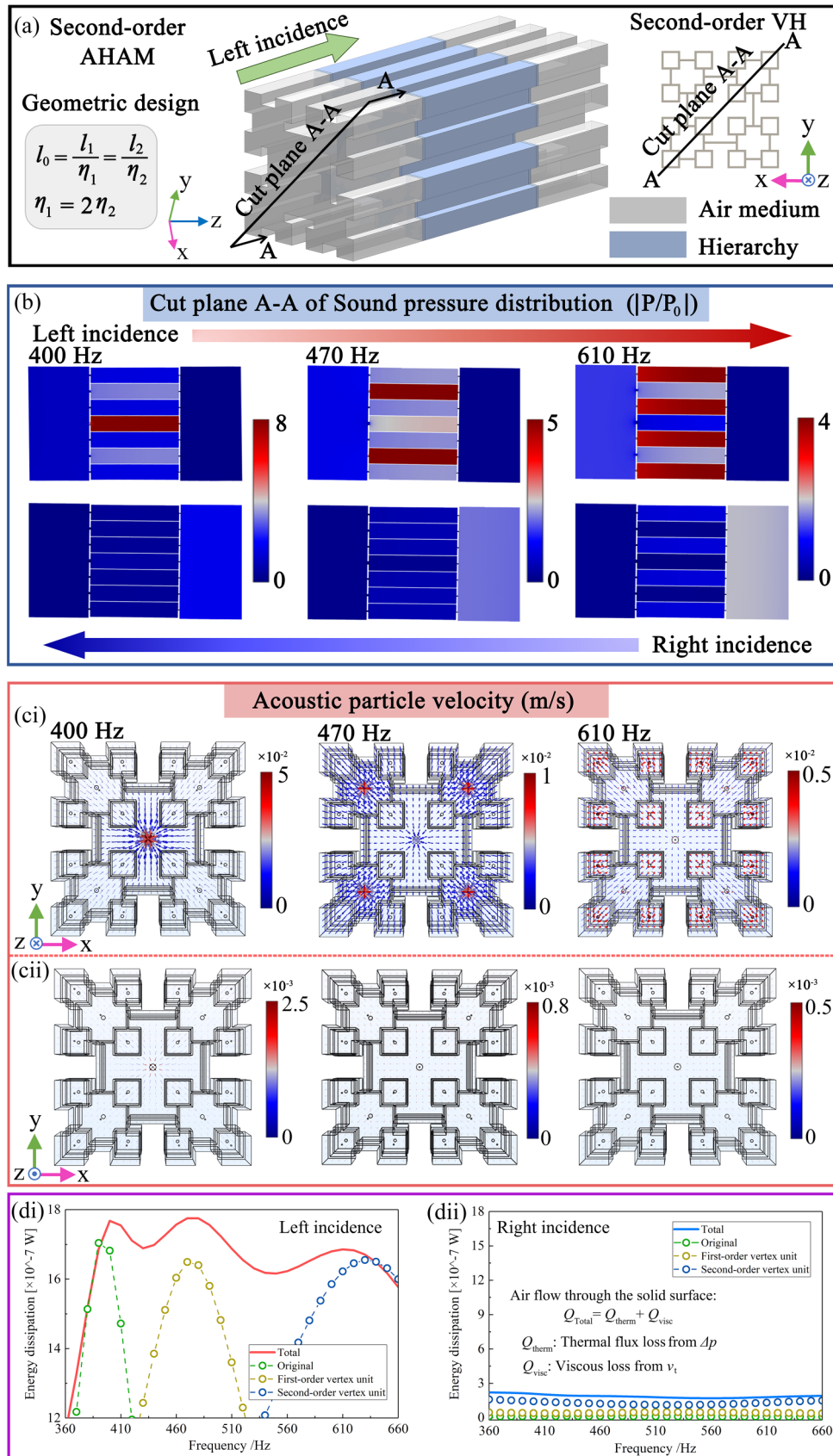


FIG. 4. Sound-absorbing behavior of second-order AHAM. (a) Simulated model of periodic second-order AHAM. (b) Cut plane of sound-pressure distributions of second-order AHAM when sound waves radiate from the left and right sides. (c) Acoustic particle velocity of second-order AHAM from (i) the left side, and (ii) the right side. (d) The quantized analysis of energy dissipation of second-order AHAM and the coupling units when working alone from (i) left and (ii) right sides.

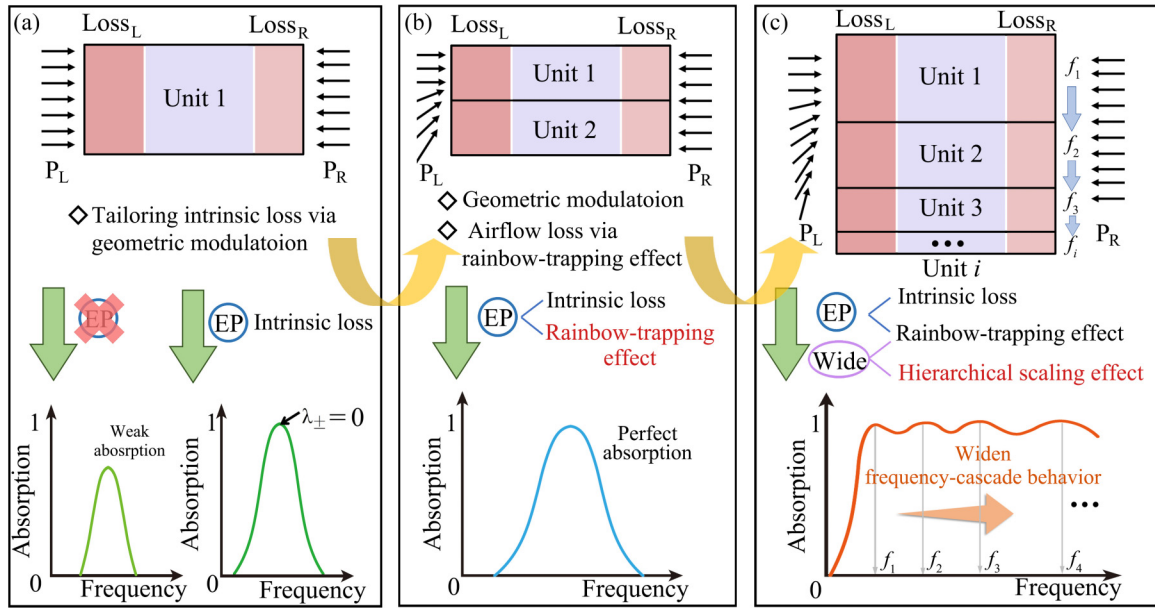


FIG. 5. Schematic views of the physical mechanism of constructing asymmetric broadband sound absorption. (a) Modulation of intrinsic loss via geometric parameters. (b) Integrated design combining intrinsic loss and additional airflow loss. (c) Hierarchical configuration for wide frequency-cascade behavior.

and quantized analysis of energy dissipation on the performance. Here, we utilize the second-order AHAM depicted in Fig. 3(c) as an example to analyze the absorption behavior at corresponding resonant frequencies. Figure 4(a) illustrates a simulated model of one periodic second-order AHAM and a schematic view of second-order VH. The gray and blue parts represent the air medium and hierarchical structure, respectively. For an intuitive view, a cut plane is used to express the sound-pressure distributions on both sides, as shown in Fig. 4(b). When the sound waves radiate from the left side, a large sound-pressure difference for frequencies corresponding to the peaks of absorption is observed, i.e., $f = [400, 470, \text{ and } 610]$ Hz. Meanwhile, the acoustic-field variations of each frequency are primarily localized in one class of resonator; that is, the prototypical cell, first-order vertex cells, and second-order vertex cells in order. The adorned hierarchical design ensures both extendable and effective sound absorption. When sound waves propagate from the right side, the acoustic field remains nearly constant, suggesting weak absorption performance.

Further, the acoustic particle velocity distributions are analyzed in Fig. 4(c) and Fig. 4(cii). Similar to the sound-pressure distributions in Fig. 4(b), the frequency-cascade and high-efficiency absorption mechanism can be illustrated via the rainbow-trapping effect [43–45]. The sound particles flow centrally to one unit due to the existence of sound-pressure difference, generating violent vibrations and absorbing all the incident energy. The rainbow-trapping effect also originates from the acoustic impedance inconsistency between different units. The unit where the particles converge exhibits well-matched impedance with air, while other units nearly resemble a sound hard boundary at the same frequency, thereby contributing to the sound-pressure difference, and a significant amount of sound energy is dissipated. The successive rainbow-trapping effect occurs at hierarchical cells

with different resonant frequencies, resulting in broadband and efficient sound absorption. The detailed rainbow-trapping mechanism is further explained by two Helmholtz resonators (HRs) in parallel in Appendix C. Meanwhile, the rainbow-trapping effect cannot be produced due to the small sound-pressure difference from the right incidence, thus exhibiting weak absorption, as shown in Fig. 4(cii).

To elaborate on the rainbow-trapping effect, showcasing exceptional pointlike characteristics within a continuous absorption band, we delve into a quantized analysis of energy dissipation in Fig. 4(d). The solid lines represent the total dissipation of second-order AHAM, while the dotted lines refer to the energy dissipation of each coupled unit when they work alone. Physically speaking, we propose two dissipation behaviors for the absorption mechanism of the rainbow-trapping model: (i) thermal dissipation of air phases; and (ii) viscous dissipation of pores. The two energy-dissipating mechanisms lead to the obvious thermoviscous effect at resonance frequencies; detailed descriptions are expressed in Appendix C.

Compared to the second-order AHAM, three single absorbers—the original unit, the first-order vertex unit, and the second-order vertex unit—exhibit weak energy dissipation. The viscous dissipation is mainly determined by the tangential velocity v_t , and the thermal loss is from Δp . The rainbow-trapping effect of second-order AHAM enhances these two metrics due to larger airflow aggregating at the corresponding resonance frequency. Combined dissipation Q_{therm} and Q_{visc} are increased ascribed to additional airflow dissipations, facilitating the synthesis of EP. Hence, the integrated approach for EP that combines intrinsic loss through loss-factor modulation with extra airflow loss via the rainbow-trapping effect enables continuous and high-efficiency sound absorption.

The physical mechanisms of processing asymmetric broadband sound absorption are exhibited in Fig. 5. EPs can be

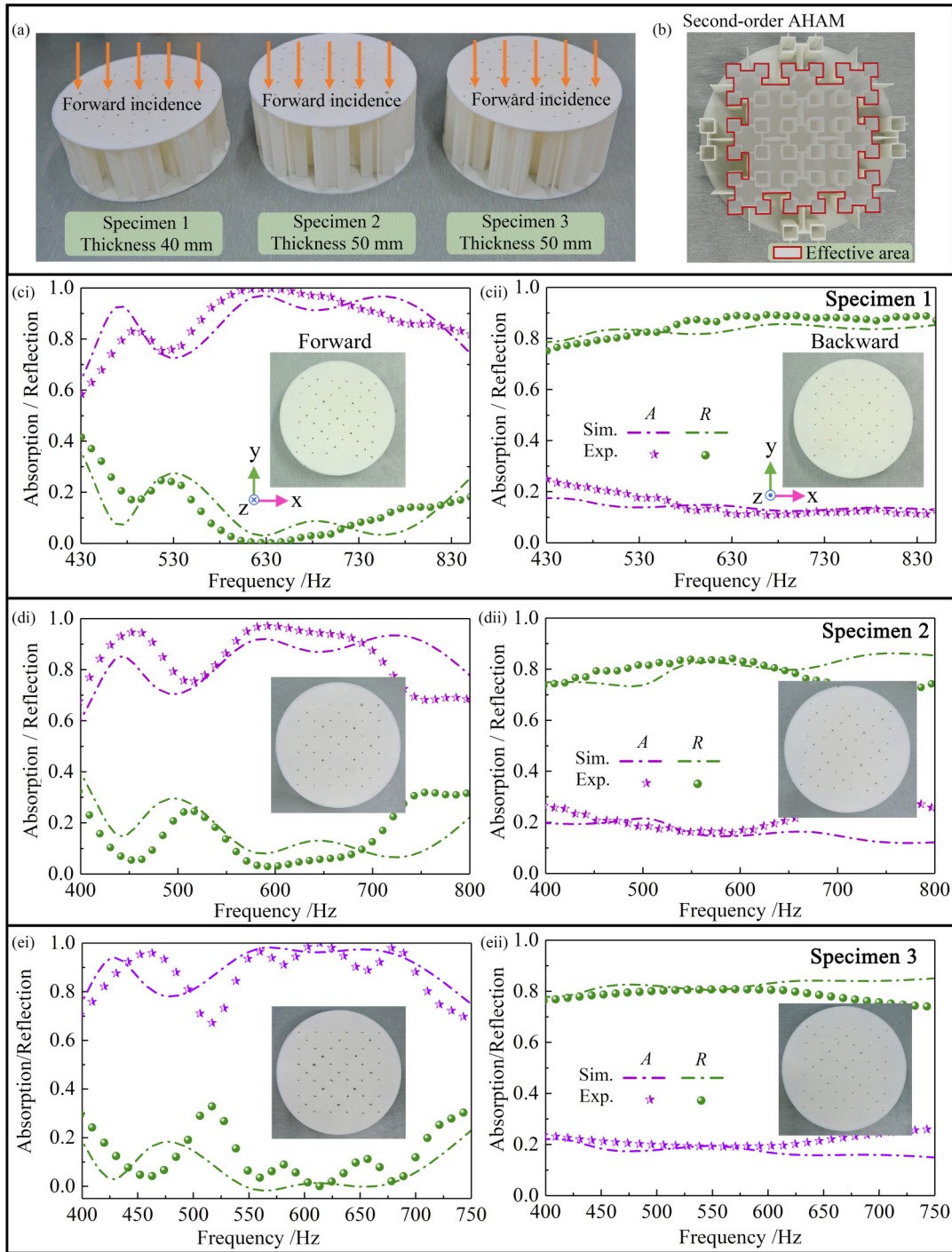


FIG. 6. (a) Photographs of second-order AHAMs with different geometric parameters. (b) The effective area of the entire specimen contains sound-absorbing ability. (c)–(e) Experimental-measured and numerically simulated sound-absorption performance and reflection spectrum of second-order AHAMs when sound waves radiate from (i) forward, and (ii) backward side.

synthesized in non-Hermitian acoustic systems with unbalanced intrinsic losses in different sections, shown in Fig. 5(a). By judiciously tailoring the loss and geometric parameters of the non-Hermitian system to reach the EP, extreme asymmetric absorption can be observed. However, achieving asymmetric responses solely through careful manipulation of structural parameters is highly limited. One viable approach is to incorporate additional lossy media into the system, but this may lead to a more sophisticated design of the system.

An integrated approach has been developed in Fig. 5(b). The rainbow-trapping effect produces additional loss via aggregating airflow, facilitating the synthesis of EP without the necessity of incorporating lossy media. Meanwhile, the parameter space utilized in Fig. 2(e) for synthesizing EP is expanded. Broadband absorption features are produced by the hierarchical configuration with graded dimensions and scaling effect, which drastically decreases the number of coupling sections and exhibits continuously expanding

TABLE III. Geometric parameters of experimental specimens (unit: mm).

	$d_{1,1}$	$d_{1,2}$	$d_{1,3}$	t_1	$d_{2,1}$	$d_{2,2}$	$d_{2,3}$	t_2	l_c	l_0	η_1	η_2
Specimen 1	1.6	1.0	0.8	1	0.5	0.45	0.35	1	38	25	0.5	0.25
Specimen 2	1.6	1.2	0.9	1	0.8	0.5	0.35	1	48	25	0.5	0.25
Specimen 3	1.6	1.2	0.8	1	0.8	0.5	0.35	1	48	25	0.5	0.25

frequency-cascade behavior, expressed in Fig. 5(c). In general, the proposed approach provides a versatile platform for other loss-induced metamaterials design.

IV. EXPERIMENTAL VERIFICATION

For our experimental implementation, compact specimens of second-order AHAMs are analyzed to illustrate the wide-band asymmetric absorption capacity. The shape of the specimens, with a diameter of 99.6 mm and a thickness of 40 mm, was designed as a cylinder to meet the dimensional requirements of the impedance tube, as shown in Fig. 6(a). The experimental setup is presented in Appendix A. The second-order AHAMs were fabricated via fused deposition modeling. Geometric parameters are listed in Table III. It should be stressed that the effective area of hierarchical configuration is shown in Fig. 6(b), which displays the completed periodic units. The negative effect on sound absorption is minimized by not perforating the flawed cells at the edge. The numerically simulated and experimentally measured sound-absorption and reflection spectra of second-order AHAMs are exhibited in Figs. 6(c)–6(e) when sound waves radiate from forward- and backward sides, respectively. The high absorption coefficients (absorption ≥ 0.7) in Fig. 6(c) are realized over a frequency range of 400 Hz with a relative bandwidth approaching 95% compared to the total measured frequency range. Meanwhile, absorption peaks are observed for the forward side from 475 to 755 Hz, achieving a deep-subwavelength scale (operating wavelength ranging from 18 to 11 times the wavelength). For the backward incidence, low absorption and high reflection were exhibited in Fig. 6(cii), achieving broadband sound-absorption asymmetry within the low-frequency realm. Furthermore, Figs. 6(d) and 6(e) shows further investigation of another specimen of second-order AHAM, achieving high-efficiency broadband sound absorption. Certainly, slight deviations observed between experiments and simulations can be attributed to geometric defects in the manufacturing and bonding processes. The effects of disorder and uncertainty introduced by these defects in the experiments primarily contribute to additional viscous-flow dissipation via resonance at pores. Detailed deviation analysis of the experiments is discussed in Appendix D. Although slight microgeometric defects in the manufacturing of the structure are inevitable, the experimental results are reliable and repeatable. Among the three outcomes, the maximum discrepancy between the experiment and simulation has a slight difference, demonstrating a high degree of conformity. Meanwhile, for the second-order AHAM, there is a significant asymmetry in sound absorption when sound waves radiate from both sides, validating the effectiveness of the proposed structure.

V. CONCLUSION

In summary, our study delved into the realm of non-Hermitian (lossy) systems and acoustic metamaterials, probing their potential for asymmetric sound absorption within the deep-subwavelength thickness of the low-frequency domain. The key to this achievement lies in our strategic manipulation of accessing the exceptional point—an integrated approach that combines intrinsic loss through loss-factor modulation with extra airflow loss via the rainbow-trapping effect to reach the EP in a loss-only system. Additionally, we introduce a vertex-based hierarchy with graded dimensions and scaling effects, showcasing an efficiency-enhanced absorption spectrum. Specifically, the proposed asymmetric hierarchical acoustic metamaterial achieves a bandwidth exceeding 400 Hz within the low-frequency spectrum at the deep-subwavelength scale when sound waves radiate from one side, accompanied by near-total reflection from the opposite side. In essence, our loss-induced design strategy empowers hierarchical metamaterials with various functionalities: asymmetry, deep-subwavelength capabilities, and high-efficiency broad absorption. The present method not only advances the manipulation of acoustic waves but also opens avenues for diverse noise-control applications.

ACKNOWLEDGMENTS

This work was supported by the National Key R&D Program of China (Grant No. 2022YFB4300101), Hunan Provincial Natural Science Foundation of China (Grant No. 2023JJ10074) and the Science and Technology Innovation Program of Hunan Province (Grant No. 2023RC1011).

APPENDIX A: NUMERICAL AND EXPERIMENTAL METHOD

The numerical model is displayed in Fig. 7(a). The gray area represents the solid phase of periodic square asymmetric absorbers, while the blue and red areas represent the air phase (the dynamic viscosity of air, $\mu = 1.8 \times 10^{-5}$ Pa · s; the static air density, $\rho = 1.2$ kg/m³; and the sound speed, $c = 343$ m/s). The propagation of sound waves is governed by pressure-acoustic module. The simulated output sound is determined by impedance, which is set as $[1.2 \text{ kg/m}^3 \times 343 \text{ m/s}]$. Due to the impedance mismatch of the air phase and the solid phase, the interfaces between the air and absorber body are treated as acoustic hard boundaries. Note that the side boundary of the pressure-acoustic module is also defined as an acoustic hard boundary. Additionally, the perforated pores are very small and experience thermal loss and viscous loss, so the thermoviscous-acoustic module is considered. The thermoviscous-acoustic layer thickness is

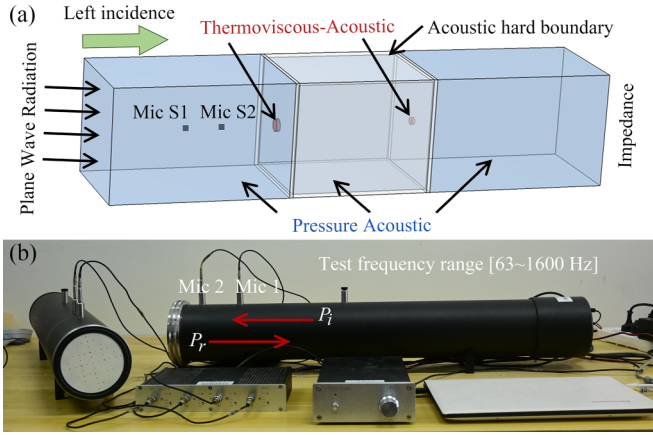


FIG. 7. (a) Finite-element model in COMSOL MULTIPHYSICS and (b) experimental setup in an impedance tube.

$d_{\text{visc}} = 0.22 \text{ mm} \times \sqrt{100/f_e}$, where f_e refers to the end frequency of the frequency domain in COMSOL. To determine the reflection, transmission, and absorption coefficients, the TMM is employed. Mic S1 and Mic S2 are utilized to measure the incident- and reflected sound pressure, respectively. The transmission coefficient is calculated by the ratio of transmitted sound power to incident sound power.

Experimental measurements were carried out using the four microphone transfer-matrix method following the standard procedure detailed in ASTM E2611-09 [63], using a large impedance tube (SKC Acoustics Technology Co Ltd type ZT13) for verification purposes. The experimental setup is depicted in Fig. 7(b). The impedance tube, with an inner diameter of 100 mm, is capable of testing frequencies ranging from 63 to 1600 Hz. During the measurements, both anechoic and rigid boundaries are achieved by opening the end cover at the waveguide's terminal, as described in Refs. [39,64]. The test piece is subjected to an incident plane wave generated by the loudspeaker, which is oriented perpendicular to its surface.

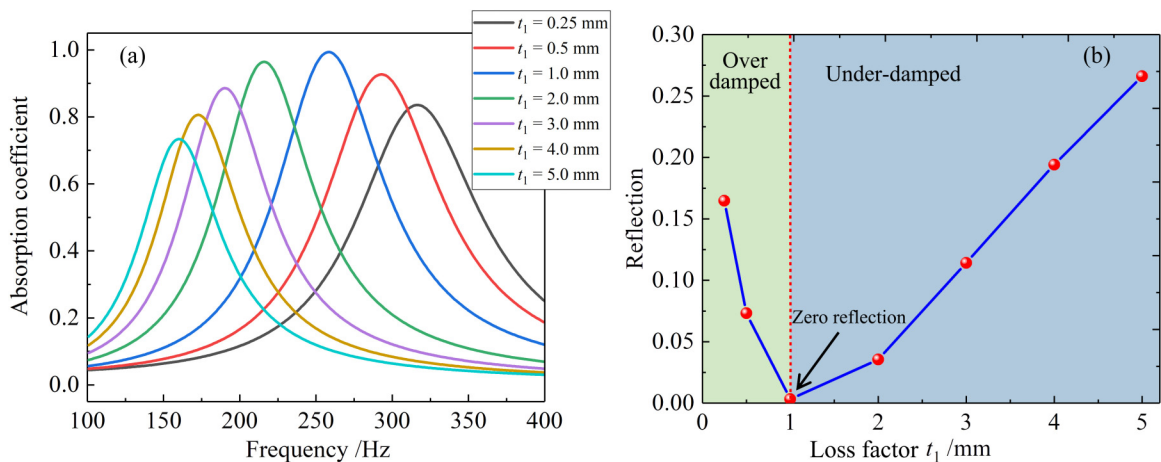


FIG. 8. Influence of the thickness t_1 of left MPP on (a) sound-absorption spectrum. (b) Reflection coefficient observation of absorption peak values.

APPENDIX B: SOUND-ABSORPTION PERFORMANCE VIA MODULATING LOSS FACTORS

Except for the diameter $d_{1,1}$ of the left MPP, other geometric factors on the sound-absorption performance are explored. First, we analyze the sound-absorption performance of the thickness t_1 of the left MPP. The maximum absorption peak is achieved when t_1 equals 1 mm and reaches an EP state, as shown in Fig. 8(a). Meanwhile, the absorption performance exhibits increasing and subsequent decreasing tendency when increasing the plates' thickness. The underlying physical mechanism is revealed in Fig. 8(b) via the observation of the reflection coefficient at absorption peak values. The increasing thickness of the left MPP goes through the overdamped state to the underdamped state, and the zero reflection occurs at the transition (critical state) where the EP emerges.

For other loss factors ($d_{2,1}$ and t_2 of secondary MPP), we conduct the analysis of the eigenvalues by obtaining EP. Here, we calculate the real part and imaginary part of eigenvalues (λ_{\pm}) of secondary MPP with different parameters, as illustrated in Fig. 9. And, the eigenvalues of the two-port acoustic system are given as $\lambda_{\pm} = T \pm \sqrt{R_l R_r}$. The EP is accessed when the real parts $\text{Re}(\lambda_{\pm})$ and corresponding imaginary parts $\text{Im}(\lambda_{\pm})$ of eigenvalues are simultaneously equal to zero, as indicated by the purple frames. Meanwhile, this tailored design also undergoes the transition from overdamped to underdamped and obtains the critical state. Hence, we can get the PA at the EP (critical) by elaborately decorating the loss factors.

APPENDIX C: PHYSICAL MECHANISM OF THE RAINBOW-TRAPPING EFFECT

To further reveal the physical mechanism of the rainbow-trapping effect, two square HRs in parallel are utilized to generate the rainbow-trapping effect, shown in Fig. 10(a). The surface acoustic impedance of HR A and HR B is Z_A and Z_B ,

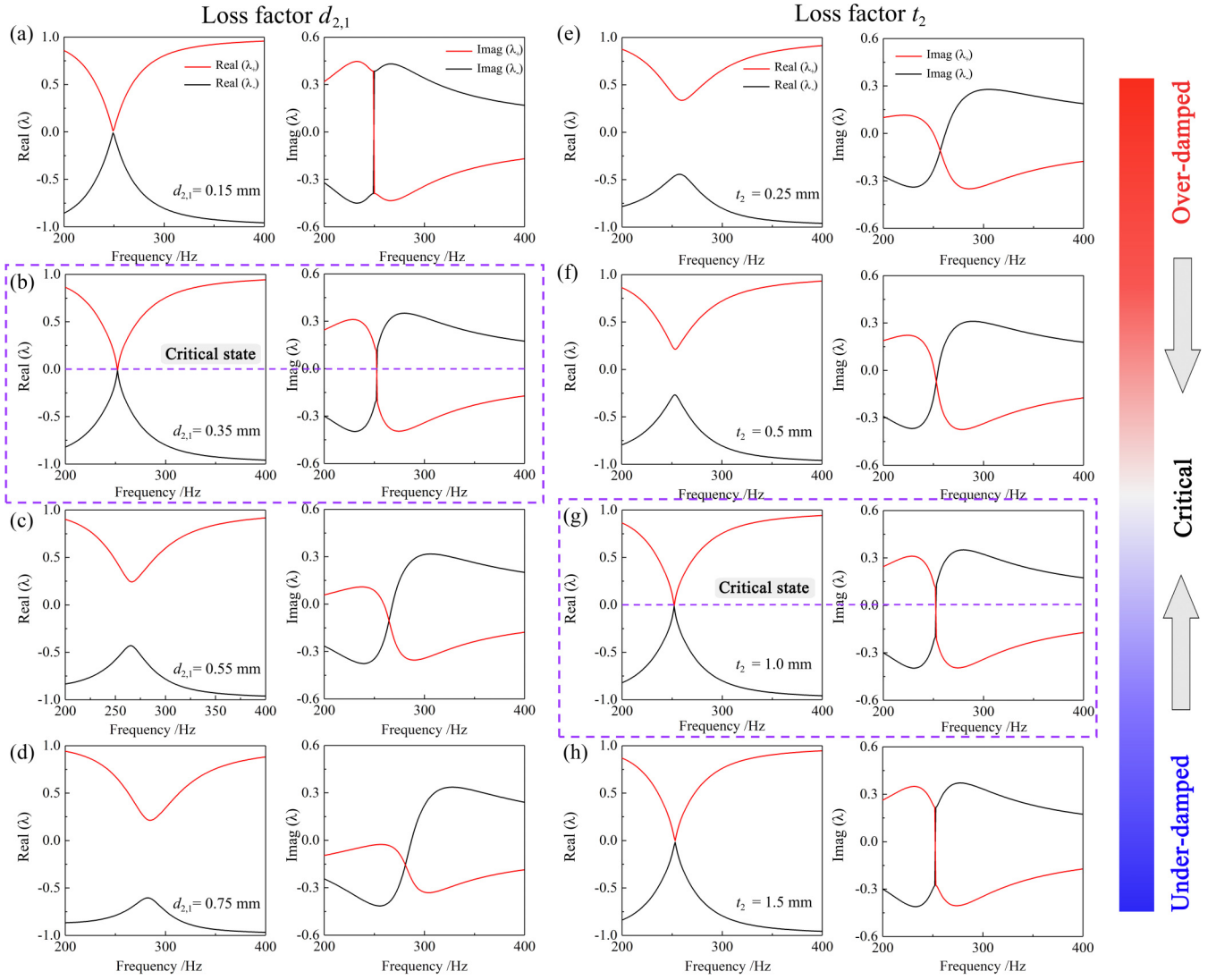


FIG. 9. Eigenvalue analysis of the acoustic asymmetric system of secondary MPP.

respectively, expressed as

$$\begin{aligned} Z_A &= R_A + jX_A, \\ Z_B &= R_B + jX_B, \end{aligned} \quad (\text{C1})$$

where R_A and R_B refer to the acoustic resistance; X_A and X_B are the acoustic reactance; and $j = \sqrt{-1}$. When the sound waves vertically radiate on the surface of the structure along the direction of the x axis, the incident sound field p_i and the reflected sound field p_r are calculated as

$$p_i = p_{ia} e^{j(\omega t - kx)}, \quad (\text{C2})$$

$$p_r = \gamma p_{ia} e^{j(\omega t + kx) + \sigma\pi}, \quad (\text{C3})$$

where p_{ia} indicates the amplitude of incident sound pressure and γ is the magnification of the acoustic pressure amplitude. $\sigma\pi$ is the phase difference between reflected and incident sound waves. The total sound-pressure field and

corresponding sound-particle velocity can be given as

$$p = p_{ia} e^{j(\omega t - kx)} + \gamma p_{ia} e^{j(\omega t + kx) + \sigma\pi}, \quad (\text{C4})$$

$$v(x, t) = (p_{ia} e^{j(\omega t - kx)} + \gamma p_{ia} e^{j(\omega t + kx) + \sigma\pi}) / Z_0. \quad (\text{C5})$$

Combining Eqs. (C1)–(C3), we can get

$$\gamma_{A,B} = \sqrt{\frac{(R_{A,B} - 1)^2 + X_{A,B}}{(R_{A,B} - 1)^2 + X_{A,B}}} \quad (\text{C6})$$

$$(\sigma\pi)_{A,B} = \arctan\left(\frac{2X_{A,B}}{R_{A,B}^2 + X_{A,B}^2 + 1}\right), \quad (\text{C7})$$

Hence, the surface sound pressure of HR A and HR B can be expressed as

$$\begin{aligned} p_A(x=0, t) &= p_{ia} e^{j\omega t} (1 + \gamma_A e^{j(\sigma\pi)_A}) \\ p_B(x=0, t) &= p_{ia} e^{j\omega t} (1 + \gamma_B e^{j(\sigma\pi)_B}). \end{aligned} \quad (\text{C8})$$

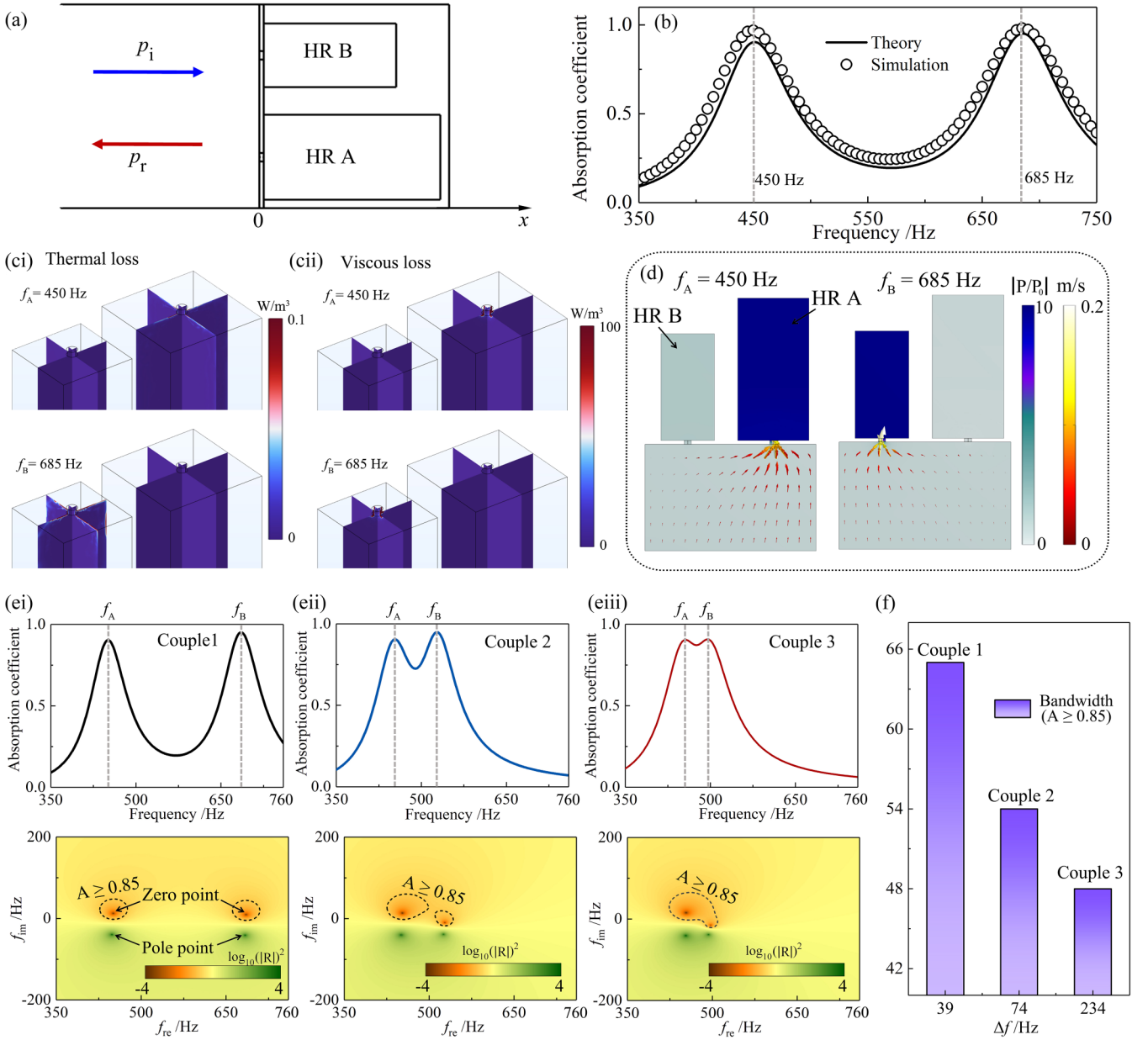


FIG. 10. (a) Schematic view of two coupling HRs and (b) corresponding sound -absorption spectrum. (c.i) and (c.ii) Energy dissipation maps of resonant frequencies. (d) Sound-pressure field and acoustic particle velocity distributions of coupling HRs at the frequencies of absorption peaks. (e.i)-(e.iii) Sound-absorption performance of different resonance frequencies and corresponding reflection coefficient in the complex frequency plane. (f) A metrical comparison of bandwidth and resonance frequency difference.

Finally, the sound-pressure difference between HR A and HR B is

$$\Delta p = p_{ia} e^{j\omega t} (\gamma_A e^{j(\sigma\pi)_A} - \gamma_B e^{j(\sigma\pi)_B}). \quad (C9)$$

According to Eq. (C9), the sound-pressure difference leads to the converging flow of sound particles, resulting in the rainbow-trapping effect. Here, the sound-absorption spectrum of the parallel coupling between HR A and HR B is exhibited in Fig. 10(b). Two quasiperfect absorption peaks are produced at 450 and 685 Hz.

The energy dissipation of two HRs is elucidated by the pressure-acoustic and thermoviscous-acoustic modules of COMSOL MULTIPHYSICS. In general, we propose two dissipation behaviors for the absorption mechanism for the

rainbow-trapping model: (i) thermal dissipation of air phases; and (ii) viscous dissipation of pores. The two energy-dissipating mechanisms lead to the obvious thermoviscous effect at the resonance frequency.

First is thermal dissipation, which refers to the breakdown of the adiabatic nature of sound propagation: where thermal flux, and hence energy converted and lost, arises from the thermal boundary layers associated with the airflow. The constituent thermal flux then leads to pressure changes and hence power dissipation with pressure in the form of [65]

$$Q_{\text{therm}} = \frac{1}{2}(\gamma - 1) \frac{p^2}{\rho_0 c_0^2} \sqrt{\frac{\omega k}{2\rho_0 C_p}}, \quad (C10)$$

where γ refers to the specific-heat ratio, p is the pressure outside of the boundary layer, k represents the thermal diffusivity, and C_p is the specific heat capacity of air. As shown in Fig. 10(c*i*), this thermal dissipation occurs mainly on the surface of cavities, and plates at corresponding resonant frequency.

The other dissipation originates from the vibration and friction of the viscous flow of air in the pores at resonance frequency. To be specific, the equation of viscous dissipation can be expressed as [65]

$$Q_{\text{visc}} = \frac{1}{2} \mu \frac{v_t^2}{\delta_{\text{visc}}}, \quad (\text{C11})$$

where $\delta_{\text{visc}} = \sqrt{2\mu/\rho_0\omega}$ denotes the viscous boundary layer, μ is the dynamic viscosity, and v_t is the tangential velocity. The energy dissipated by vibration-induced friction loss at resonances is schematically depicted in Fig. 10(c*ii*). The air vibrates in the vicinity of the microperforations; hence, the sound energy is converted into heat and the incident sound intensity is diminished. The consequence is that from the logscale color bar, it can be observed that loss due to thermal flux is significantly lower than that by the viscous flow, consistent with the design principles. From the total thermal-viscous dissipation, the primary contributor is the viscous loss in the pores, while the contributed thermal dissipation in the cavities is negligible.

Further, the sound-pressure distributions and particle velocity of corresponding frequencies are exhibited in Fig. 10(d) to illustrate the absorption behavior. The acoustic impedance of HR B at 685 Hz approximately satisfies the matching conditions, so the value of acoustic resistance is 1 and the acoustic reactance is 0. HR A has almost no sound-absorption performance, which can be equivalent to the sound hard boundary, so the maximum sound-pressure difference can be obtained from HR B. The particles flow to the HR B due to the large sound pressure that occurs at the HR B, and this phenomenon is called the rainbow-trapping effect. Note that the absorbing behavior of HR A also exhibits the same property.

Through the above-mentioned analysis, it can be seen that only when the energy concentration phenomenon in the acoustic rainbow-trapping effect occurs, the sound-absorbing structure can fully absorb the incident sound energy without producing reflected sound waves, and finally achieve excellent sound-absorption performance. Hence, the acoustic rainbow-trapping effect can be regarded as the basic physics mechanism for all parallel sound-absorbing structures to achieve high-efficiency broadband sound absorption.

Furthermore, the absorption spectra and coupling strength of the HR system are theoretically calculated by varying the pore diameter of HR B, as shown in Fig. 10(e). When the difference in resonance frequencies between HR A and HR B is significant, two discrete absorption peaks are observed. Plotting the reflection coefficient (R) in the complex frequency plane by decomposing the complex frequency $f_c = \text{Re}(f_c) + \text{Im}(f_c)i$, provides more physical insight into the absorption performance of absorber [14–16]. Two discrete pairs of zero and pole shift downwards due to the losses of the system.

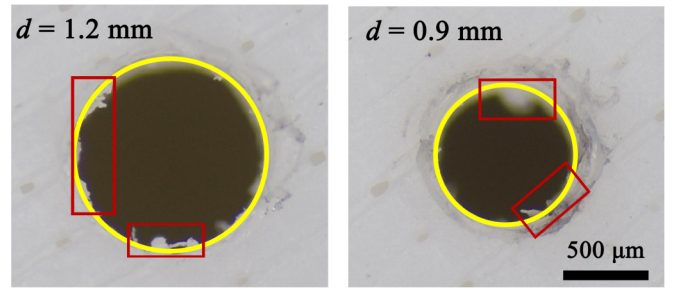


FIG. 11. Representative images of the fabrication defects.

The critical coupling condition is nearly fulfilled (the intrinsic loss perfectly balances the leaked energy), i.e., both zeros are located near the real frequency axis. However, the two pairs of zero and pole are located far apart from each other, and the contour lines (describing $A \geq 0.8$ wholly illustrates the high-efficiency absorption domain) are isolated, indicating a weak interaction coupling effect between them. By adjusting the resonance frequencies of alternative resonators to be closer to each other, shown in Figs. 10(e*ii*)–10(e*iii*), the absorption valley becomes smoother, and the high-efficiency absorption domain is widened. Further, the sound-absorber system with continuous broadband bandwidth is achieved due to the overlapping of two absorption peaks. The enhancements in the absorption bandwidth can be ascribed to the strong coupling of two inhomogeneous HRs with adjacent resonance frequencies, producing a flat high-efficiency absorption.

A metrical comparison is provided in Fig. 10(f). As shown, the relationship between the first resonance frequency difference of HRs ($\Delta f = f_B - f_A$) and bandwidth ($A \geq 0.85$) is consistent with the enhanced absorption performance observed in the HRs with different coupling strengths.

APPENDIX D: EXPERIMENTAL DEVIATION ANALYSIS

The deviations observed between the experiments and simulations are primarily attributed to geometric defects in the manufacturing process. These manufacturing defects may lead to disorder effects and introduce uncertainty into the experimental results. Figure 11 exhibits two typical pores of specimens, where there are filamentous and elliptical sections (outlined in red) along the vertical portion of the structure in the form of branches, which effectively reduce the effective pore sizes [8,66,67]. The main contribution to overall sound absorption lies with viscous-flow dissipation via resonance at the pores. Energy dissipation at the matching pores is observed to be higher than that in the cavity. Therefore, the structural cavity is not expected to significantly contribute to viscous losses. All these, along with the absorption performance when decreasing the pore size, result in lower resonance behavior. The roughness of the pores where viscous loss occurs leads to intensified friction between the airflow and the structural surface, resulting in increased dissipation and high absorption coefficients.

- [1] N. Gao, Z. Zhang, J. Deng, X. Guo, B. Cheng, and H. Hou, Acoustic metamaterials for noise reduction: A review, *Adv. Mater. Technol.* **7**, 2100698 (2022).
- [2] Y. Tao, M. Ren, H. Zhang, and T. Peijs, Recent progress in acoustic materials and noise control strategies –A review, *Appl. Mater. Today* **24**, 101141 (2021).
- [3] M. Yang and P. Sheng, Acoustic metamaterial absorbers: The path to commercialization, *Appl. Phys. Lett.* **122**, 260504 (2023).
- [4] S. Qu, Y. Hou, and P. Sheng, Conceptual-based design of an ultrabroadband microwave metamaterial absorber, *Proc. Natl. Acad. Sci. USA* **118**, e2110490118 (2021).
- [5] K. Y. Bliokh, Y. P. Bliokh, V. Freilikher, S. Savel'Ev, and F. Nori, *Colloquium: Unusual resonators: Plasmonics, metamaterials, and random media*, *Rev. Mod. Phys.* **80**, 1201 (2008).
- [6] Z. Li, X. Li, Z. Wang, and W. Zhai, Multifunctional sound-absorbing and mechanical metamaterials via a decoupled mechanism design approach, *Mater. Horiz.* **10**, 75 (2023).
- [7] A. Fernandez-Marin, N. Jimenez, J. Groby, J. Sanchez-Dehesa, and V. Romero-Garcia, Aerogel-based metasurfaces for perfect acoustic energy absorption, *Appl. Phys. Lett.* **115**, 061901(2019).
- [8] X. Li, X. Yu, and W. Zhai, Additively manufactured deformation-recoverable and broadband sound-absorbing microlattice inspired by the concept of traditional perforated panels, *Adv. Mater.* **33**, 2104552 (2021).
- [9] Z. Li, X. Wang, X. Li, Z. Wang, and W. Zhai, New class of multifunctional bioinspired microlattice with excellent sound absorption, damage tolerance, and high specific strength, *ACS Appl. Mater. Interfaces* **15**, 9940 (2023).
- [10] K. Zeng, Z. Li, Z. Guo, X. Liang, and Z. Wang, Acoustic metamaterial for highly efficient low-frequency impedance modulation by extensible design, *Extreme Mech. Lett.* **56**, 101855 (2022).
- [11] F. Ma, C. Wang, Y. Du, Z. Zhu, and J. H. Wu, Enhancing of broadband sound absorption through soft matter, *Mater. Horiz.* **9**, 653 (2022).
- [12] K. Zeng, Z. Li, Z. Guo, and Z. Wang, Reconfigurable and phase-engineered acoustic metasurfaces for broadband wavefront manipulation, *Adv. Phys. Res.* 2300128 (2024).
- [13] X. Li, X. Yu, J. W. Chua, and W. Zhai, Harnessing cavity dissipation for enhanced sound absorption in Helmholtz resonance metamaterials, *Mater. Horiz.* **10**, 2892 (2023).
- [14] S. Huang, Z. Zhou, D. Li, T. Liu, X. Wang, J. Zhu, and Y. Li, Compact broadband acoustic sink with coherently coupled weak resonances, *Sci. Bull.* **65**, 373 (2020).
- [15] C. Shao, Y. Zhu, H. Long, C. Liu, Y. Cheng, and X. Liu, Metasurface absorber for ultra-broadband sound via over-damped modes coupling, *Appl. Phys. Lett.* **120**, 083504 (2022).
- [16] V. Romero-García, G. Theocharis, O. Richoux, A. Merkel, V. Tournat, and V. Pagneux, Perfect and broadband acoustic absorption by critically coupled sub-wavelength resonators, *Sci. Rep.* **6**, 19519 (2016).
- [17] S. Huang, Y. Li, J. Zhu, and D. P. Tsai, Sound-absorbing materials, *Phys. Rev. Appl.* **20**, 010501 (2023).
- [18] G. Ma and P. Sheng, Acoustic metamaterials: From local resonances to broad horizons, *Sci. Adv.* **2**, e1501595 (2016).
- [19] B. Assouar, B. Liang, Y. Wu, Y. Li, J. C. Cheng, and Y. Jing, Acoustic metasurfaces, *Nat. Rev. Mater.* **3**, 460 (2018).
- [20] S. A. Cummer, J. Christensen, and A. Alù, Controlling sound with acoustic metamaterials, *Nat. Rev. Mater.* **1**, 16001 (2016).
- [21] X. Zhang, T. Zhang, M.-H. Lu, and Y.-F. Chen, A review on non-Hermitian skin effect, *Adv. Phys.: X* **7**, 2109431 (2022).
- [22] H. Ge, M. Yang, C. Ma, M. H. Lu, Y. F. Chen, N. Fang, and P. Sheng, Breaking the barriers: Advances in acoustic functional materials, *Natl. Sci. Rev.* **5**, 159 (2018).
- [23] H. Nassar, B. Yousefzadeh, R. Fleury, M. Ruzzene, A. Alù, C. Daraio, A. N. Norris, G. Huang, and M. R. Haberman, Nonreciprocity in acoustic and elastic materials, *Nat. Rev. Mater.* **5**, 667 (2020).
- [24] G. U. Patil, S. Cui, and K. H. Matlack, Leveraging nonlinear wave mixing in rough contacts-based phononic diodes for tunable nonreciprocal waves, *Extreme Mech. Lett.* **55**, 101821 (2022).
- [25] C. Rasmussen, L. Quan, and A. Alù, Acoustic nonreciprocity, *J. Appl. Phys.* **129**, 210903 (2021).
- [26] Z. Chen, Y. Peng, H. Li, J. Liu, Y. Ding, B. Liang, X. Zhu, Y. Lu, J. Cheng, and A. Alù, Efficient nonreciprocal mode transitions in spatiotemporally modulated acoustic metamaterials, *Sci. Adv.* **7**, eabj1198 (2021).
- [27] Z. Gu, H. Gao, P. Cao, T. Liu, X. Zhu, and J. Zhu, Controlling sound in non-Hermitian acoustic systems, *Phys. Rev. Appl.* **16**, 057001 (2021).
- [28] X. Wu, L. Wang, S. Chen, X. Chen, and L. Yuan, Transition characteristics of non-Hermitian skin effects in a zigzag lattice without chiral symmetry, *Adv. Phys. Res.* **2**, 2300007 (2023).
- [29] V. Achilleos, G. Theocharis, O. Richoux, and V. Pagneux, Non-Hermitian acoustic metamaterials: Role of exceptional points in sound absorption, *Phys. Rev. B* **95**, 144303 (2017).
- [30] S. K. Gupta, Y. Zou, X. Zhu, M. Lu, L. Zhang, X. Liu, and Y. Chen, Parity-time symmetry in non-Hermitian complex optical media, *Adv. Mater.* **32**, 1903639 (2020).
- [31] C. Shen, J. Li, X. Peng, and S. Cummer, Synthetic exceptional points and unidirectional zero reflection in non-Hermitian acoustic systems, *Phys. Rev. Mater.* **2**, 125203 (2018).
- [32] A. Guo and G. J. Salamo, Observation of \mathcal{PT} -symmetry breaking in complex optical potentials, *Phys. Rev. Lett.* **103**, 093902 (2009).
- [33] K. Ding, G. Ma, Z. Q. Zhang, and C. T. Chan, Experimental demonstration of an anisotropic exceptional point, *Phys. Rev. Lett.* **121**, 085702 (2018).
- [34] R. El-Ganainy, K. G. Makris, M. Khajavikhan, Z. H. Musslimani, S. Rotter, and D. N. Christodoulides, Non-Hermitian physics and PT symmetry, *Nat. Phys.* **14**, 11 (2018).
- [35] Ş. K. Özdemir, S. Rotter, F. Nori, and L. Yang, Parity-time symmetry and exceptional points in photonics, *Nat. Mater.* **18**, 783 (2019).
- [36] C. Shi, M. Dubois, Y. Chen, L. Cheng, H. Ramezani, Y. Wang, and X. Zhang, Accessing the exceptional points of parity-time symmetric acoustics, *Nat. Commun.* **7**, 11110 (2016).
- [37] J. Li, Y. Jing, and S. A. Cummer, Nonreciprocal coupling in space-time modulated systems at exceptional points, *Phys. Rev. B* **105**, L100304 (2022).
- [38] C. Wang, W. R. Sweeney, A. D. Stone, and L. Yang, Coherent perfect absorption at an exceptional point, *Science* **373**, 1261 (2021).

- [39] H. Long, C. Shao, Y. Cheng, J. Tao, and X. Liu, High absorption asymmetry enabled by a deep-subwavelength ventilated sound absorber, *Appl. Phys. Lett.* **118**, 263502 (2021).
- [40] J. W. Jung, J. E. Kim, and J. W. Lee, Acoustic metamaterial panel for both fluid passage and broadband soundproofing in the audible frequency range, *Appl. Phys. Lett.* **112**, 041903 (2018).
- [41] H. Long, Y. Cheng, and X. Liu, Asymmetric absorber with multiband and broadband for low-frequency sound, *Appl. Phys. Lett.* **111**, 143502 (2017).
- [42] T. Lee, T. Nomura, E. M. Dede, and H. Iizuka, Asymmetric loss-induced perfect sound absorption in duct silencers, *Appl. Phys. Lett.* **116**, 214101 (2020).
- [43] N. Jiménez, V. Romero-García, V. Pagneux, and J. P. Groby, Rainbow-trapping absorbers: Broadband, perfect and asymmetric sound absorption by subwavelength panels for transmission problems, *Sci. Rep.* **7**, 13595 (2017).
- [44] J. Zhu, Y. Chen, X. Zhu, F. J. Garcia-Vidal, X. Yin, W. Zhang, and X. Zhang, Acoustic rainbow trapping, *Sci. Rep.* **3**, 1728 (2013).
- [45] H. Wu, Y. Yin, Z. Sheng, Y. Li, D. Qi, and R. Peng, Multiband omnidirectional ventilated acoustic barriers based on localized acoustic rainbow trapping, *Phys. Rev. Appl.* **15**, 054033 (2021).
- [46] Z. Wang, Z. Guo, Z. Li, and K. Zeng, Design, manufacture, and characterisation of hierarchical metamaterials for simultaneous ultra-broadband sound-absorbing and superior mechanical performance, *Virtual Phys. Prototypes* **18**, e2111585 (2022).
- [47] Z. Wang, Z. Guo, Z. Li, and K. Zeng, Coupling and scaling effect for low-frequency broadband sound absorption via vertex-based hierarchy, *Appl. Phys. Lett.* **119**, 171903 (2021).
- [48] Z. Li, Z. Wang, Z. Guo, X. Wang, and X. Liang, Ultrabroadband sound absorption of a hierarchical acoustic metamaterial at high temperatures, *Appl. Phys. Lett.* **118**, 161903 (2021).
- [49] J. Pierre, F. Iervolino, R. D. Farahani, N. Piccirelli, M. Lévesque, and D. Therriault, Material extrusion additive manufacturing of multifunctional sandwich panels with load-bearing and acoustic capabilities for aerospace applications, *Addit. Manuf.* **61**, 103344 (2023).
- [50] Z. Li, W. Zhai, X. Li, X. Yu, Z. Guo, and Z. Wang, Additively manufactured dual-functional metamaterials with customizable mechanical and sound-absorbing properties, *Virtual Phys. Prototypes* **17**, 864 (2022).
- [51] D. Saatchi, S. Oh, and I. Oh, Biomimetic and biophilic design of multifunctional symbiotic Lichen-Schwarz metamaterial, *Adv. Funct. Mater.* **33**, 2214580 (2023).
- [52] P. Fratzl and R. Weinkamer, Nature's hierarchical materials, *Prog. Mater. Sci.* **52**, 1263 (2007).
- [53] Z. Tang, N. Kotov, S. Magonov, and B. Ozturk, Nanostructured artificial nacre, *Nat. Mater.* **2**, 413 (2003).
- [54] K. Verdière, R. Panneton, S. Elkoun, T. Dupont, and P. Leclaire, Transfer matrix method applied to the parallel assembly of sound absorbing materials, *J. Acoust. Soc. Am.* **134**, 4648 (2013).
- [55] D. Y. Maa, Potential of microperforated panel absorber, *J. Acoust. Soc. Am.* **104**, 2861 (1998).
- [56] Y. Zhu, H. Long, C. Liu, H. Zhang, Y. Cheng, and X. Liu, An ultra-thin ventilated metasurface with extreme asymmetric absorption, *Appl. Phys. Lett.* **120**, 141701 (2022).
- [57] D. Li, S. Huang, Y. Cheng, and Y. Li, Compact asymmetric sound absorber at the exceptional point, *Sci. China-Phys. Mech. Astron.* **64**, 244303 (2021).
- [58] K. Ding, G. Ma, M. Xiao, Z. Q. Zhang, and C. T. Chan, Emergence, coalescence, and topological properties of multiple exceptional points and their experimental realization, *Phys. Rev. X* **6**, 021007 (2016).
- [59] Y. Long, H. Xue, and B. Zhang, Non-Hermitian topological systems with eigenvalues that are always real, *Phys. Rev. B* **105**, L100102 (2022).
- [60] W. Zhu, X. S. Fang, D. T. Li, Y. Sun, Y. Li, Y. Jing, and H. Chen, Simultaneous observation of a topological edge state and exceptional point in an open and non-Hermitian acoustic system, *Phys. Rev. Lett.* **121**, 124501 (2018).
- [61] X. Wang, X. Fang, D. Mao, Y. Jing, and Y. Li, Extremely asymmetrical acoustic metasurface mirror at the exceptional point, *Phys. Rev. Lett.* **123**, 214302 (2019).
- [62] Z. Zhou, S. Huang, D. Li, J. Zhu, and Y. Li, Broadband impedance modulation via non-local acoustic metamaterials, *Natl. Sci. Rev.* **9**, nwab171 (2022).
- [63] ASTM-E2611-09, *Standard Test Method for Measurement of Normal Incidence Sound Transmission of Acoustical Materials Based on Transfer Matrix Method* (ASTM International, West Conshohocken, PA, 2009).
- [64] B. H. Song and J. S. Bolton, A transfer-matrix approach for estimating the characteristic impedance and wave numbers of limp and rigid porous materials, *J. Acoust. Soc. Am.* **107**, 1131 (2000).
- [65] M. J. Cops, J. G. McDaniel, E. A. Magliula, and D. J. Bamford, Analysis of thermal and viscous boundary layers in acoustic absorption by metallic foam, *J. Acoust. Soc. Am.* **146**, 649 (2019).
- [66] J. Boulvert, J. Costa-Baptista, T. Cavalieri, M. Perna, E. R. Fotsing, V. Romero-García, G. Gabard, A. Ross, J. Mardjono, and J.-P. Groby, Acoustic modeling of micro-lattices obtained by additive manufacturing, *Appl. Acoust.* **164**, 107244 (2020).
- [67] X. Li, J. W. Chua, X. Yu, Z. Li, M. Zhao, Z. Wang, and W. Zhai, 3D-Printed lattice structures for sound absorption: Current progress, mechanisms and models, structural-property relationships, and future outlook, *Adv. Sci.* **11**, 2305232 (2023).